MBE technology of semiconductor quantum well lasers

KAZIMIERZ REGIŃSKI*, MACIEJ BUGAJSKI

Institute of Electron Technology, Warsaw, Poland

In this paper we concentrate mainly on technological problems related to the growth of graded-refractive index separate−confinement heterostructure single quantum well (GRIN SCH SQW) lasers. This technology is still a challenge for molecular beam epitaxy (MBE) laboratories because of many delicate problems connected with the growth process. By analyzing surface reconstruction for GaAs and $Al_{0.3}Ga_{0.7}As$ at the static conditions and during the growth of respective layers we were able to construct phase diagrams for MBE, which allowed us to specify the optimum growth conditions in terms of growth temperature and molecular fluxes. Despite the difficulties encountered, molecular beam epitaxy is particularly suitable for preparing laser structures because it allows one to control precisely layer thickness, produce heterointerfaces with monolayer abruptness and vary chemical composition profiles with a high degree of precision.

In order to better understand the physical processes taking place in the QW lasers as well as to optimize the technological parameters of their manufacturing process we apply a conventional threshold analysis. The spectral dependence of gain is calculated from the first principles; than confinement properties are studied in terms of layer composition and thickness. Design criteria are derived, which minimize the threshold current of GRIN SCH SQW lasers. On the basis of these optimization rules AlGaAs/GaAs lasers were fabricated and tested.

1. Introduction

The recent installation of the three chamber, modular molecular beam epitaxy (MBE) system (Riber 32P), at the Institute of Electron Techno-logy, has made possible to grow various low dimensional structures important for device applications in optoelectronics. In this paper we concentrate mainly on technological problems connected with growing the graded-refractive index separate−confinement heterostructure (GRIN SCH) lasers. This technology is still a challenge for MBE laboratories because of many delicate problems connected with the growth process.

* corresponding author: Kazimierz Regiński, Institute of Electron Technology, Al. Lotników 32/46, 02-668 Warsaw, Poland.

Despite the problems they pose, AlGaAs/GaAs GRIN SCH single quantum well (SQW) lasers continue to receive an increasing interest due to their special properties associated with a two-dimensional nature of carriers confined in the quantum well active region. In almost every aspect the quantum well lasers are somewhat better than conventional lasers with bulk active regions. The main advantages of quantum well lasers are wavelength tunability and more gain per injected carrier resulting in lower thresholds and possibility to generate more power. They also show narrower linewidths, higher speed and less temperature sensitivity [1]. Molecular beam epitaxy (MBE) is particularly suitable for preparing laser structures because it allows one to precisely control layer thickness, produce heterointerfaces with monolayer abruptness and vary chemical composition profiles with a high degree of precision [2]. In order to better understand the physical processes taking place in the QW lasers as well as to optimize the technological parameters of their manufacturing process we apply a conventional threshold analysis [3–6]. The gain calculations follow generally the formalism of Chinn et al. [7] with some extensions. Confinement properties are studied in terms of layer composition and thickness. Design criteria are derived, which minimize the threshold current of GRIN SCH SQW lasers. On the basis of these optimization rules, AlGaAs/GaAs lasers were fabricated and tested.

An example of such a structure (with a single quantum well) is presented in Fig. 1. The diagram shows simultaneously the Al content in the layers composing the structure, the dopant concentration throughout the structure, and the substrate temperature during the growth of the separate layers. The GRIN SCH SQW structures were grown on a (100)- oriented n^+-GaAs substrate. The sequence of layers was initiated by GaAs buffer layer followed by a GaAs/$Al_{0.7}Ga_{0.3}$As superlattice and n-type AlGaAs confinement layer. The active region consisted of a GaAs quantum well bounded by two Al_xGa_{1-x}As GRIN regions with Al content varying between 0.25 and 0.70. The top confinement layer was of p-type and was followed by a contact structure. The contact structure has been composed of three different layers: a heavily doped p-type GaAs layer, a quasi-metalic Be layer, and Al metallic layer which could be formed either *ex-situ* or *in-situ* by MBE [8]. The thickness of the individual layers and the level of doping as well as the doping profile were subjected to changes in different types of lasers during the optimization process. In that sense the values of parameters of the GRIN SCH SQW structure shown in Fig. 1 should be understood as an example (one of the possible optimum combinations of the parameters). More information about details of construction of GRIN SCH SQW lasers can be found in our recent papers [9–12].

2. Molecular beam epitaxy growth system

The growth processes reported in this study have been performed by ES MBE (Elemental Source Molecular Beam Epitaxy) technique on RIBER 32P machine equipped with ABN 135L evaporation cells. Certain details of the control systems installed in the growth chamber of this machine are presented in Fig. 2. It should be pointed out that all crucial measurements necessary for monitoring the growth conditions (substrate temperature and molecular fluxes) were performed directly. Substrate temperature was measured with an IRCON pyrometer and additionally by a thermocouple. The molecular fluxes were measured by a Bayard-Alpert gauge mounted on the sample manipulator. The manipulator could be rotated so as to place the Bayard-Alpert gauge at the standard position of the substrate. Thus the gauge could measure the beam equivalent pressure of the As_4 beam. This pressure, in turn, was converted to the absolute value of flux by using the well–known formula [13]:

$$\frac{J_X}{J_Y} = \frac{P_X}{P_Y} \cdot \frac{\eta_Y}{\eta_X} \left(\frac{T_X M_Y}{T_Y M_X} \right)^{1/2} \qquad (1)$$

where J_N is the flux of species N (N = X,Y); P_N is its beam equivalent pressure, and T_N and M_N are the absolute temperature of the effusion cell and molecular weight of the species, respectively and η_N is the relative ionization efficiency.

For determination of the absolute value of arsenic flux we followed a standard procedure. First,
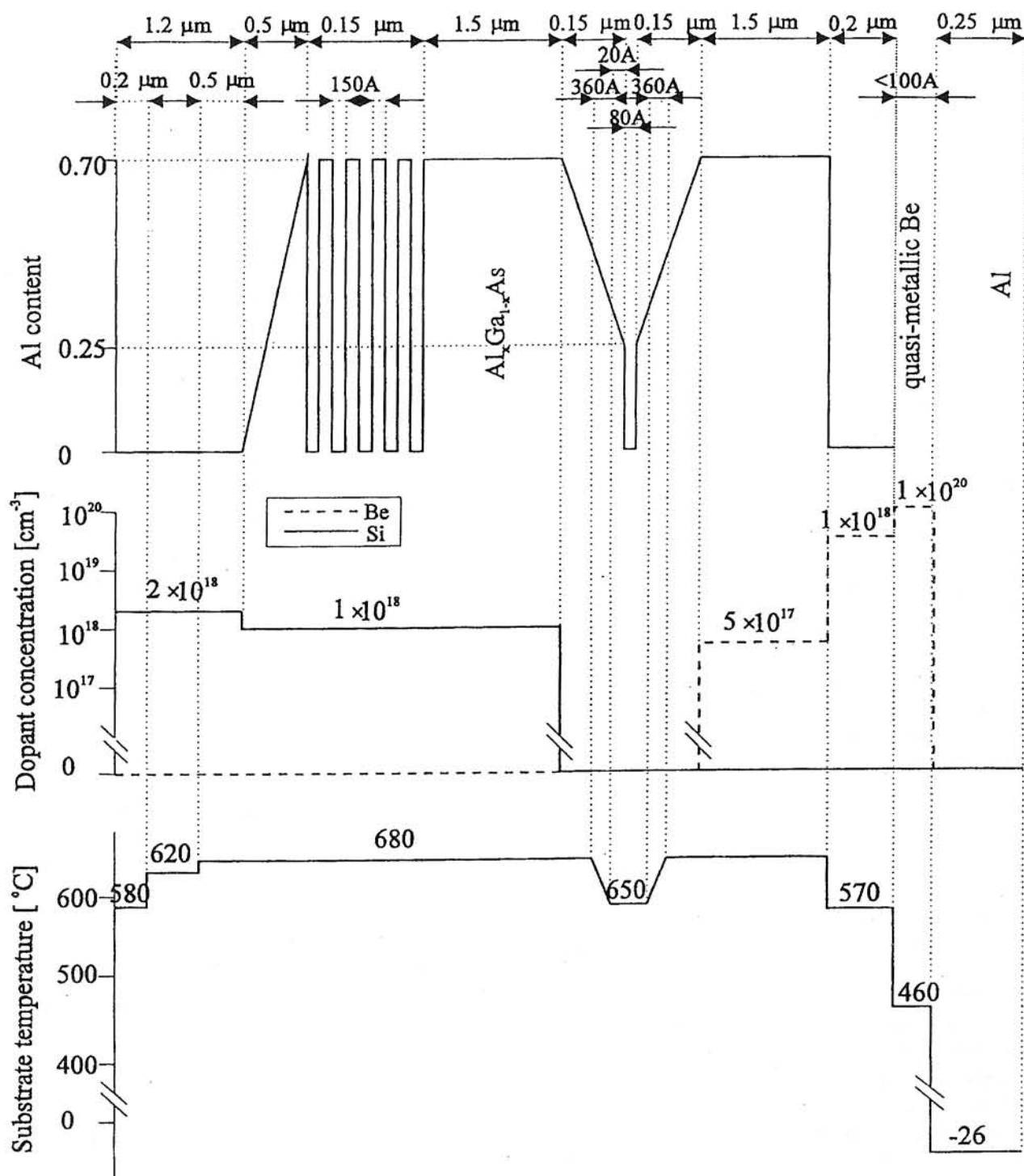
Fig. 1. Scheme of GRIN-SCH SQW laser structure grown by MBE. Al metallic layer is formed in-situ in the same process.

we calculated from the growth rate of GaAs the flux J_{Ga} during the growth process under the standard growth conditions (assuming the sticking coefficient for Ga = 1). Then from the formula (1) we calculated the flux J_{As} for the temperature of arsenic cell corresponding to the assumed growth conditions. In order to obtain the value of the arsenic flux for given temperature T'_{As} we apply the formula (1) to the case when X corresponds to the arsenic flux from the cell
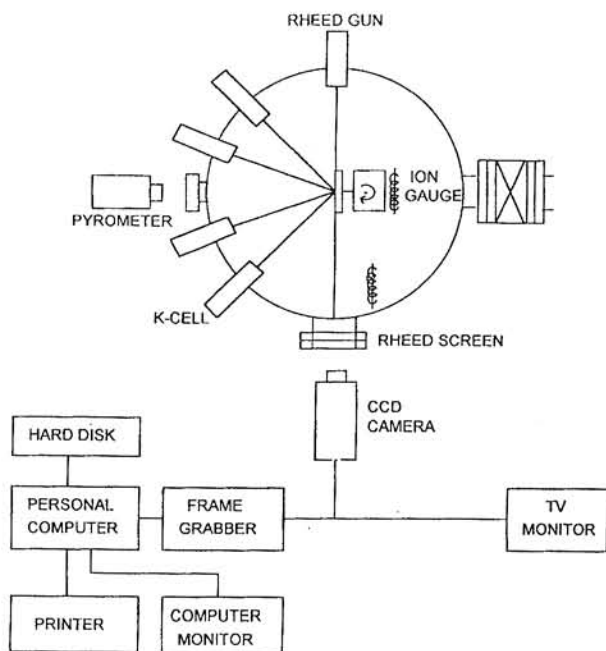
Fig. 2. *Experimental set-up for controlling the MBE process. The system for registering and processing the RHEED pattern is shown in details.*

working at the temperature T'_{As} and Y corresponds to the arsenic flux from the cell working at the temperature T_{As}.

To monitor the state of the crystal surface at any stage of the growth process the RHEED system with a 10 keV electron gun was used. The RHEED patterns were registered by CCD camera and then processed in real time and recorded by a specially built computer acquisition system (see Fig. 2) which was our addition to the standard MBE sustem supplied by the producer. It consisted of a personal computer equipped with a frame grabber, two CRT monitors, and a high resolution laser printer for capturing RHEED images. The RHEED pictures could be processed by a specially written computer program and stored on a hard disk for further reference. The system enabled us to register RHEED intensity oscillations and, as a result, to determine the growth rate v. As a result, we had at our disposal two independent methods of measuring the growth rate. The first one based on the measurement of atomic fluxes and the second one based on registering the RHEED intensity oscillations. That additional possibility strengthened our control over growth process and turned out to be crucial in developing the technology of laser structures.

3. Optimization of the growth conditions of GaAs/AlGaAs structures

The performance and reliability of semiconductor lasers depends critically on the crystal-growth technique. In this respect, lasers are probably the most demanding III−V minority carrier devices. Fabrication of high quality laser structures by MBE needs a careful optimization of the growth conditions. From the point of view of MBE technology several factors are of great importance: high purity and structure perfection of undoped layers, the relevant profiles of dopant concentration, good quality of interfaces, high dopant concentration in contact layers, etc. Therefore, the optimization of the MBE proces comprises the determination of the growth conditions for each layer of the laser structure.

The main physical parameters describing any MBE growth process are the substrate temperature T, the values of atomic fluxes $J(E_i)$ for the elements E_i, $i = 1, 2, . . ., n$, and the growth rate v, itself being the function of the former parameters. In our opinion, the best method of formulating the growth conditions is to determine them as a specific point on the so-called phase diagram of surface reconstruction. The phase diagrams show the reconstruction of atomically clean surface as a function of its temperature and atomic fluxes falling on it [14]. In the case when surface reconstruction is observed in the static conditions (without growth) the only parameters determining the reconstruction are T and $J(As_4)$. During the growth the surface reconstruction depends additionally on the fluxes $J(Ga)$ and/or $J(Al)$.

For optimization of the growth conditions of the laser structures a lot of work has been done for preparing phase diagrams for different semiconductor compounds at various growth rates [15, 16]. Some of them are presented in Figs. 3−6.

The static surface phase diagram for GaAs(001) is presented in Fig. 3. The phase boundaries divide the plane of the diagram into four regions for which the reconstructions (2x2), (2x4), (3x1), and (4x2) are seen. Together with the reconstruction (3x1) in the same region also the reconstruction (3x6) is seen. The points of phase transitions without any arsenic flux (the lowest points in the diagram) correspond to the temperatures 395°C, 495°C, and 552°C.
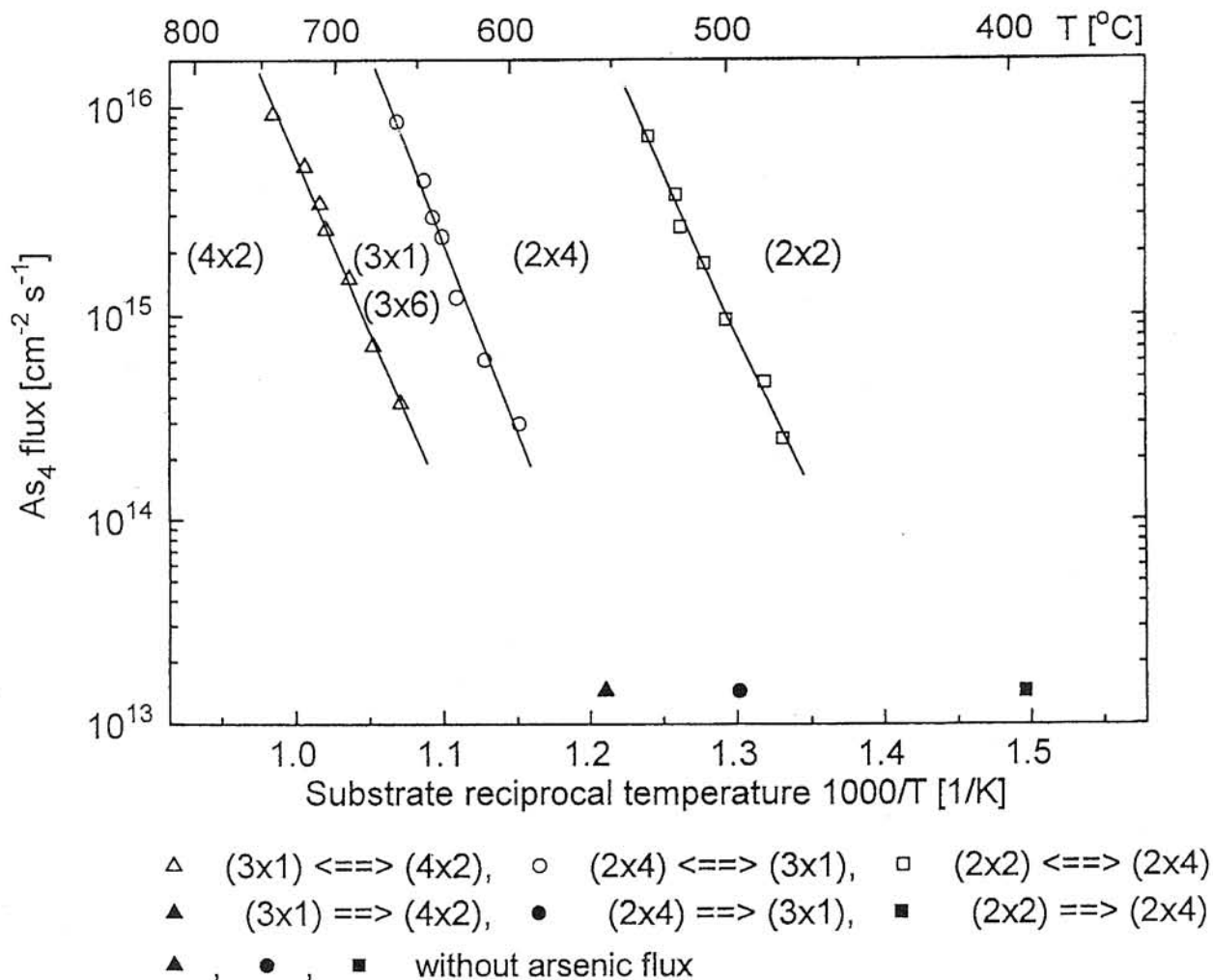
Fig. 3. Static phase diagram for GaAs (001) surface. The surface reconstructions are plotted versus the substrate temperature T and the absolute value of the As₄ flux. For the points of phase transitions without arsenic flux only the values of abscissae have a physical meaning.

The surface reconstructions during the growth of GaAs(001) were studied for the temperature range from 350°C until 770°C and for three values of the Ga flux, i.e., $1.3 \times 10^{14} cm^{-2}s^{-1}$, $6.2 \times 10^{14} cm^{-2}s^{-1}$, and $1.6 \times 10^{15} cm^{-2}s^{-1}$. For low and medium substrate temperatures (below 630°C) these values correspond to the growth rates 0.2 μm/h, 1.0 μm/h, and 2.5 μm/h, respectively. The important finding, with great practical consequence, is that the form of surface diagrams depends strongly on the growth rate [16]. One has to take this into account when designing the optimum conditions for the growth of complex multilayer structures. As an example, the surface phase diagram for GaAs (001) during the growth with the standard rate 1.0 μm/h is presented in Fig. 4. The phase boundaries divide the plane of the diagram into four regions where the reconstructions (2x2), (2x4), (3x1), and (4x2) are seen. In the same region where the reconstruction (3x1) was observed also the reconstructions (3x6) and (4x6) were seen. In the dynamic surface diagram (Fig. 4) in contrast to the static one each phase boundary curve can be divided into two parts: (1) the upper part where As₄ flux is much higher than Ga flux and (2) the lower one where As₄ flux is roughly two times Ga flux.

Similar set of diagrams has been prepared for the $Al_xGa_{1-x}As(001)$ surfaces for various compositions x and growth rates v. For illustration, Fig. 5 presents a static phase diagram and Fig. 6 a dy-
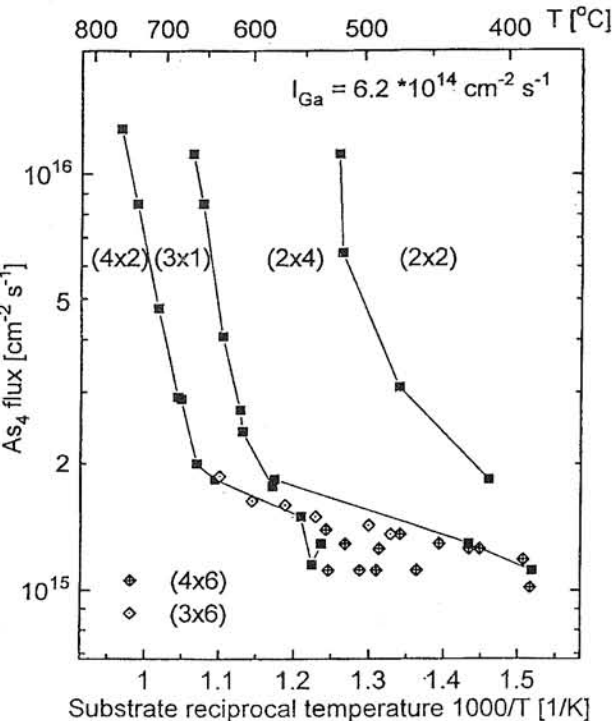
Fig. 4. The MBE phase diagram for GaAs (001) surface during the growth for the fixed Ga flux of $6.2 \times 10^{14} cm^{-2} s^{-1}$. It corresponds to the growth rate of 1.0 $\mu m/h$ in the low temperature regime. The surface reconstructions are plotted versus the inverse of the substrate temperature T and the absolute value of the As$_4$ flux.

layers in our MBE system are the following: For AlGaAs the substrate temperature $T = 680°C$, the growth rate $v = 0.5$ $\mu m/h$ and $J(As_4)/[J(Al) + J(Ga)] = 2$. For GaAs the relevant values are $T = 680°C$, the growth rate $v = 1$ $\mu m/h$ and $J(As_4)/J(Ga) = 5$. In the case of growing the whole laser structure these values have to be modified because of various additional circumstances. For instance, it should be taken into account that the high substrate temperature increases the dopant interdiffusion, the process to be avoided while growing laser structures containing higly doped emiters situated next to nominaly undoped active layers. It is also impossible to change beam fluxes abruptly. Due to the time lag of the effusion cells an unintentional doping of the structure and undesired composition fluctuations may occur.

A total number of about 30 GRIN SCH SQW laser structures were grown in the process of optimization of technology. As a result of these studies the CW room-temperature GRIN SCH SQW lasers ($\lambda = 820$ nm), with extrapolated threshold currents densities as low as 350A/cm^2 and internal quantum efficiencies of 96% were produced [9]. The lasers represent state-of-the-art in the technology of this type of devices.

namic one for $Al_{0.3}Ga_{0.7}(001)$ surface. The notations used in Fig. 5 and Fig. 6 are the same as in the case of GaAs(001) surface phase diagrams. Having the set of appropriate phase diagrams for different compounds and for various growth rates we were able to determine the relevant growth conditions for each layer of the laser structure. It is well established that the quality of MBE grown layers is mainly determined by the reconstruction of the crystal surface during the growth. The reconstruction in turn is a function of the substrate temperature and atomic fluxes. So, having the phase diagrams we can vary separately the growth parameters while still retaining in the particular surface reconstruction type. We can specify the ranges of allowed values of growth parameters for preferred type of surface reconstruction.

Analyzing surface phase diagrams we have determined that the optimum growth conditions on (2x4) reconstructed surfaces for different types of

4. Basic design rules for quantum well lasers

In this Section we will present basic design principles of quantum well lasers based on both carrier and optical confinement considerations. A typical quantum well laser consists of undoped active/wavequide region and doped emiter/cladding layers for carrier injection. The active/waveguiding layers have lower bandgaps and higher refractive index than cladding layers. Light can than be confined in the active/waveguiding region which behaves as a dielectric waveguide. Thus, both carriers and the light are confined. A significant improvement in laser parameters brought about by the introduction of separate carrier and light confinement is fully utilized in SCH QW lasers of which the most mature construction is GRIN SCH SQW laser considered here.
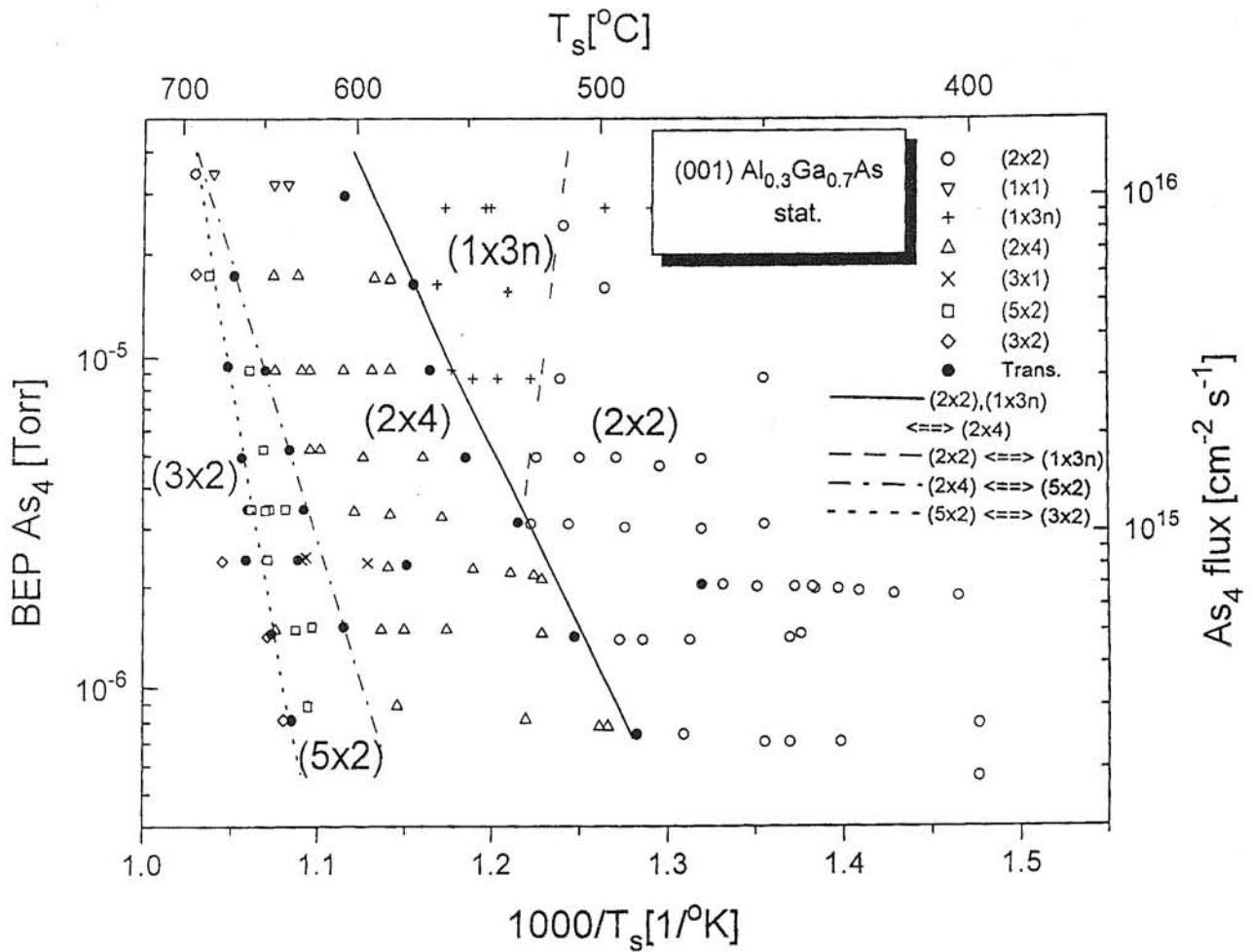
Fig. 5. Static phase diagram for $Al_{0.3}Ga_{0.7}As(001)$ surface. The surface reconstructions are plotted versus the substrate temperature T and the As_4 flux. Both the beam equivalent pressure (BEP) and the absolute value of flux are shown.

4.1. Threshold analysis of quantum well lasers

One of the fundamental quantities that describes the behaviour of an injection laser is the threshold current density J_{th}. The threshold current density J_{th} of AlGaAs/GaAs broad area Fabry-Perot lasers can be described by [3]:

$$J_{th}(A / cm^2) = \frac{J_0 d}{\eta_i} + \frac{d}{\eta_i \beta \Gamma}\alpha_i + \frac{d}{\eta_i \beta \Gamma}\frac{1}{L}\ln\frac{1}{R} \quad (2)$$

The J_{th} of the laser is due to three different contributions. The first term is the intrinsic term. The second is the internal loss term and the third is mirror loss term. The gain-current relation assumes the linear form:

$$g_{max} = \beta(J_{nom} - J_0) \quad (3)$$

In the above equations, d is the active layer thickness, η_i is the internal quantum efficiency at threshold, α_i includes all the internal losses, Γ is the optical confinement factor, L is the cavity length, R is the power reflectance of the mirror, g_{max} is the gain coefficient, β is the differential gain coefficient, J_{nom} is the nominal current density for $1\mu m$ thick active layer and unity quantum efficiency, J_0 is the transparency current density, i.e., the current density at the onset of negative absorption (gain). The internal loss term is given by:

$$\alpha_i = \Gamma\alpha_{ic} + (1 - \Gamma)\alpha_{ic,c} + \alpha_s + \alpha_c \quad (4)$$

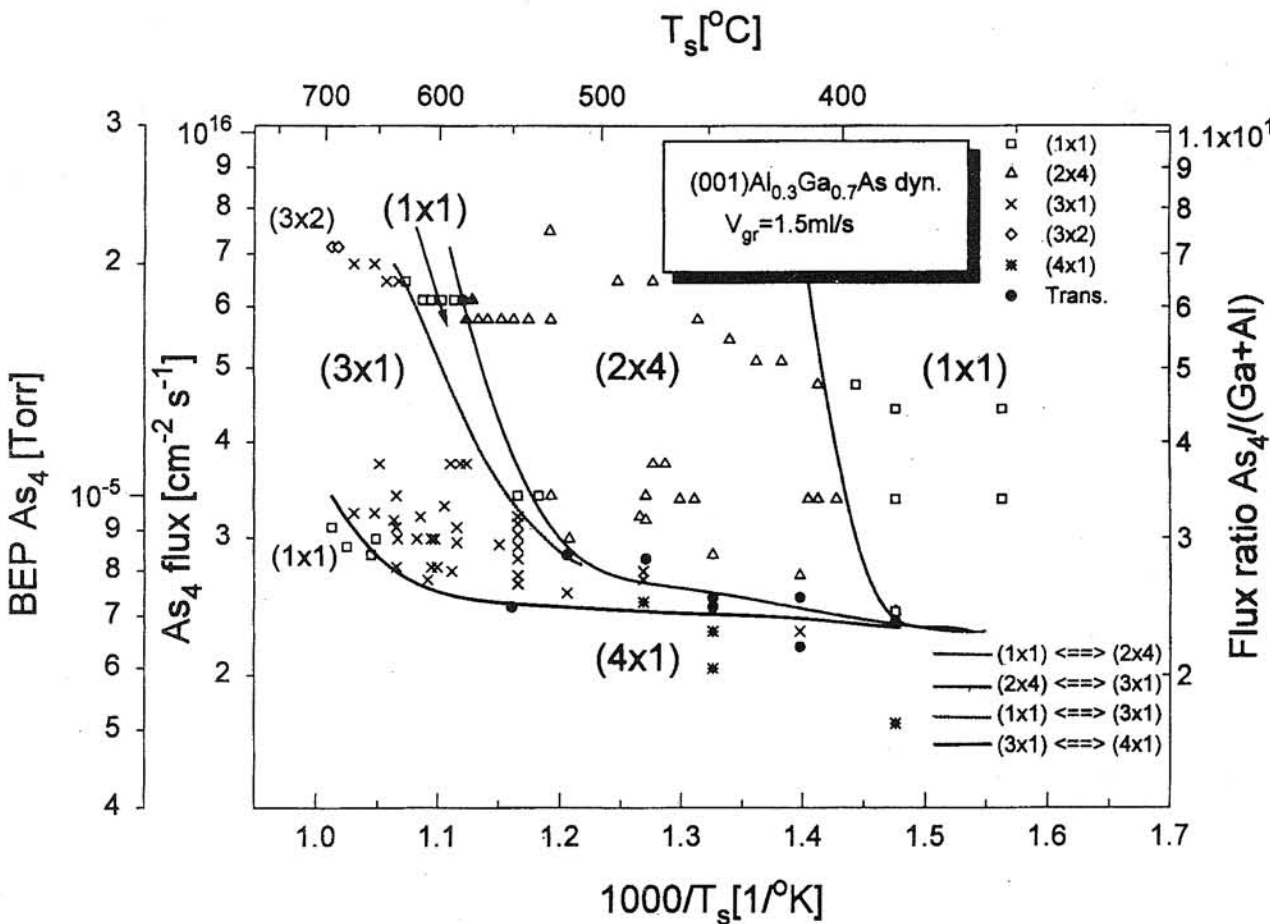*Fig. 6. The MBE phase diagram for Al$_{0.3}$Ga$_{0.7}$As(001) surface during the growth for the growth rate 1.5 µm/h. The beam equivalent pressure (BEP), the absolute value of As$_4$ flux as well as flux ratio are shown.*

In Eq.4 α_{ic} is the free-carrier absorption loss in the active layer and at the threshold it is ~ 10 cm^{-1}, $\alpha_{ic,c}$ is the free-carrier loss in the adjacent layers and for the doping concentrations ($\sim 5 \times 10^{17} - 10^{18}$ cm^{-3}) it is $\sim 5-10$ cm^{-1}, α_s is the optical scattering loss due to irregularities at the heterointerfaces which can be safely neglected in a good quality MBE grown structures. The same is true for the last term, α_c which is the coupling loss term and accounts for optical field spread beyond the cladding layers. In our design the cladding layers are thick enough to make it negligible. In quantum well lasers two last terms in Eq.2, internal loss term and mirror loss term dominate due to the small values of confinement factors Γ related to the narrow active regions. The electromagnetic field confinement to the electrically pumped active region depends on the order of the transverse mode, thickness of the active region and on the refractive index profile of the waveguiding region (quantum well plus graded composition regions on its both sides). In a broad contact laser the problem of calculating transverse mode distribution becomes essentially a one-dimensional and reduces to solving the Helmholtz equation for the field amplitude perpendicular to the junction plane. For the refactive index profile referring to GRIN SCH SQW laser this has to be done numerically (no analytical solution can be found). We have used a finite-difference method to calculate fundamental transverse mode distribution in the structure. The transverse mode field distributions for GRIN SCH SQW laser structures with different cladding layer compositions are shown in Fig. 7. The mode appears to be practically confined to the GRIN region but Γ is very low, equal to only 0.015

Fundamental Mode Intensity Distribution Perpendicular to Junction Plane
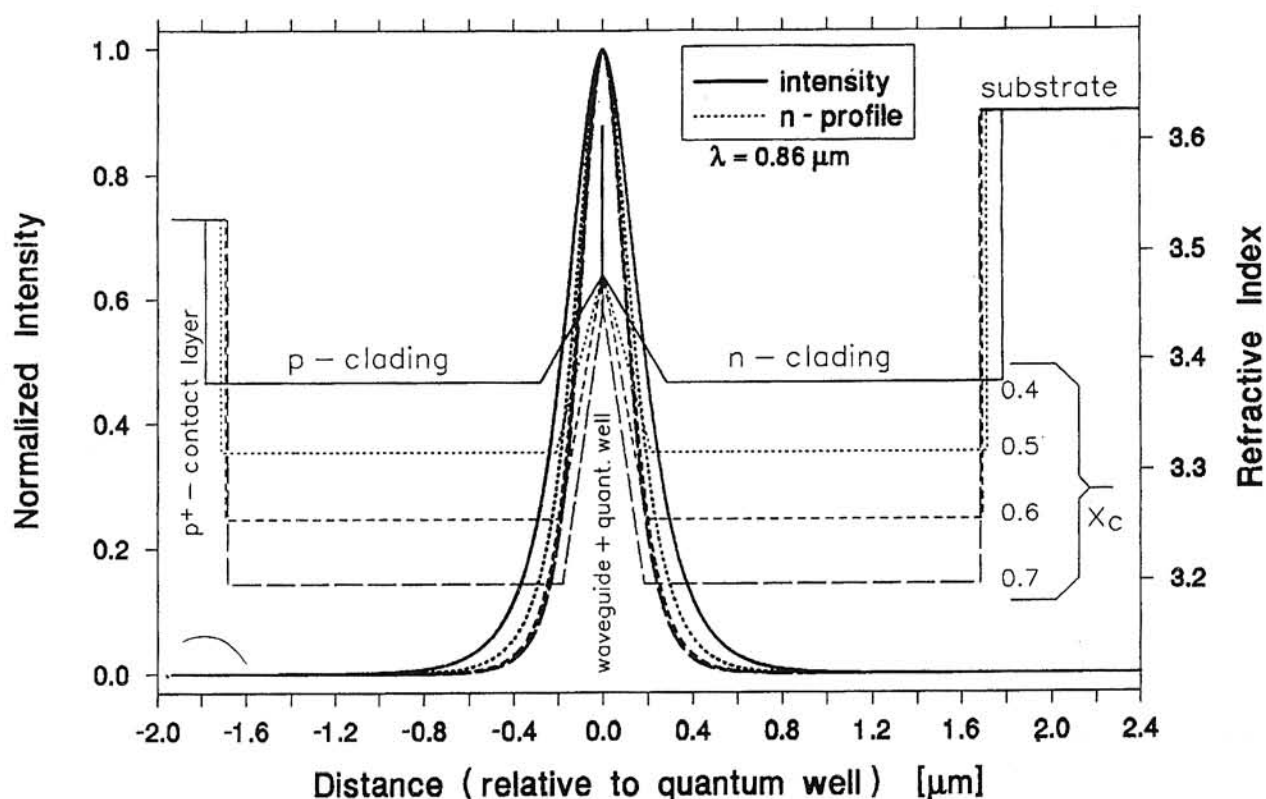## (at the optimum waveguide thickness)

Fig. 7. The transverse mode field distributions for GRIN SCH SQW laser structures with different cladding layer compositions.

because of the narrow, typically 50Å thick active region. Using the above value of confinement factor, estimated internal losses $\alpha_i = 7.5$ cm^{-1} and the internal quantum efficiency $\eta_i = 0.95$ we can calculate threshold current density for the laser structure studied and for specified resonator length L. We have assumed linear gain model as given by Eq.3. The values of J_0 and ß were taken after Tsang [17] and Wagner [18]. They represent averaged values for good GRIN SCH SQW lasers. The values of threshold current density J_{th} = 500−550 Å/cm^2 were obtained, depending on the particular choice of input parameters (see Fig. 8). The J_{th} values represent theoretical lowest limit for the laser structure considered in this paper. In practice one should not be surprised getting higher values from the experiment. On the other hand it has to be pointed out that in the light of recent findings [19, 20], the logarithmic gain

model rather than linear model appears to be more appropriate for quantum well lasers. The gain-current relation can be approximated by expression:

$$g_{max} = ßJ_0 \ln (J_{nom} / J_0) \qquad (5)$$

This in turn results in substantial lowering of theoretical threshold current density which as can be seen from Fig. 8 goes down to 150−200 Å/cm^2 range for typical construction parameters of the structure. Concluding, the calculated absolute values of threshold current density can serve as a sort of general guidance in designing lasers, especially when different structures are compared.

4.2. The optical gain model

With no carrier injection the active layer material is strongly absorbing. With carrier injection we

K. Regiński and M. Bugajski

Threshold Characteristics of GRIN-SCH-SQW LDs

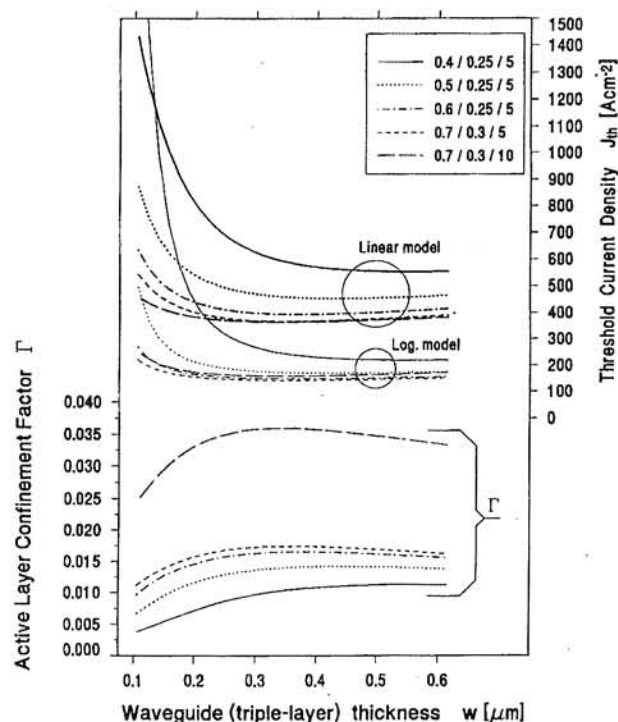Legend: clading comp./ min. waveguide comp./ quant. well thickness [nm]

Fig. 8. Threshold current density and active layer confinement factor for GRIN SCH SQW laser.

can invert the carrier population near the band edge and convert absorption into gain. The region of positive gain exists in limited energy range above the bandgap of the material. It extends between the bandgap and the quasi-Fermi level separation: $E_g < h\nu < \Delta E_F$.

The spectral shape of the QW gain and peak gain on injected carrier density differ considerably from that of bulk material. These differences are the consequences of the step-like density of states in QW material.

The optical gain is calculated using standard perturbation theory (Fermi's Golden Rule). Following the approach of Chinn at al. [7] the spectrally dependent gain coefficient can be written in the form:

$$g(E) = \frac{q^2|M|^2}{E\varepsilon_0 m^2 c h N L_z} \sum_{i,j} m_{r,ij} C_{ij} A_{ij} [f_c - (1-f_v)]$$
$$\times\, H(E - E_{ij}) \qquad (6)$$

where: $|M|^2$ – bulk momentum transition matrix element; C_{ij} – spatial overlap factor between sta-

tes i and j; A_{ij} – anisotropy (polarisation) factor for transition i,j; $m_{r,ij}$ – spatially weighted reduced mass for transition i,j; E_{ij} – transition energy between states i and j; N – effective refractive index; H – Heaviside step function; i, j – conduction, valence (lh, hh) quantum numbers at Γ point. For the perfectly confined QW states $\Delta n = 0$ selection rule applies. However, in the present case we also consider transitions between the states in the GRIN region. For those states a nonzero overlap exists between the electron and hole states of differing quantum number and i = j selection rule is no longer imposed. The reduced mass parameter is given by: $m_{r,ij}^{-1} = m_i^{-1} + m_j^{-1}$, where m_i and m_j are weighted (by wavefunction confinement factor in QW) averages of QW and cladding (GRIN) masses.

Momentum conservation restricts the energies of the initial and final states. The bulk averaged momentum matrix element between the conduction $<s|$ and valence $|x>$ states is:

$$|M|^2 = \frac{m^2 E_g (E_g + \Delta_{so})}{6 m_c (E_g + 2\Delta/3)} \qquad (7)$$

where: Δ_{so} – spin-orbit splitting parameter.

The angular anisotropy factor is normalized so that its angular average (bulk limit) is unity. For the TE transitions, with the electric field vector in the plane of the QW, its values are: $A_{ij} = 3/4(1 + \cos^2\theta_{ij})$ for e – hh transitions and $A_{ij} = 1/4(5 - 3\cos^2\theta_{ij})$ for e – lh transitions [21]. The bands are assumed to be parabolic, thus the occupation density of the ith (conduction or valence) band is:

$$n_i, p_i = \frac{kT m_i^{c,v}}{\pi\hbar^2 L_z} \ln\left[1 + \exp\left(\frac{E_f^{c,v} - E_i^{c,v}}{kT}\right)\right] \qquad (8)$$

where the quasi-Fermi energies E_f and the quantum levels E_i are measured positive into respective band from the k = 0 band edge. We assume undoped QW with high injection, so the charge neutrality gives the condition $n = p_{lh} + p_{hh}$. The effect of carrier intraband scattering is taken into account by assuming that each individual transition contributing to the gain is itself broadened by scattering and has a Lorentzian lineshape. The net effect of this broadening can be found by convolving the Lorentzian shape function with calculated from Eq.6 gain distribution $(g'(E) = g(E)*L(E))$.

The equations discussed above give the material gain of quantum well in terms of carrier density, which is not directly measurable. From the point of view of calculating properties of semiconductor injection laser the relation between the current and carrier density must be established by balancing current with total carrier recombination rate which consists of radiative and nonradiative components [22]. The radiative component of carrier recombination is found from spectrally dependent spontaneous emission rate:

$$R(E) = \frac{16\pi^2 Nq^2 E|M|^2}{\varepsilon_0 m^2 c^3 h^4 L_z} \sum_{i,j} m_{r,ij} C_{ij} [f_c f_v] H(E - E_{ij})$$

(9)

The nonradiative contribution to the current comes mainly from thermal leakage current and from Auger recombination. The most common method of estimating Auger recombination is to use experimentally obtained Auger coefficients in combination with calculated carrier density ($R_A = CN^3$). Theories can predict Auger rate to within an order of magnitude. In quantum-well lasers carriers can leak into separate confinement waveguiding layers as well as leak out of the entire SCH waveguide region into the doped cladding layers. Carrier population in the SCH region leads to recombination giving leakage current density of the order of 50Å/cm^2 per 10^{17}cm^{-3} of carrier density. This shows the importance of maintaining low carrier density in the waveguide regions of the laser.

Using the model outlined above the gain spectra of GRIN SCH SQW laser shown in Fig. 9 were calculated. The fundamental transverse mode confinement factor Γ this time is slightly higher because of the thicker quantum well, but still is low comparing to conventional DH lasers. As can be seen from Fig. 10 it reaches the value of 0.0287 for triple layer (GRIN$^-$-QW-GRIN$^+$) thickness equal to 0.454 μm. Using the values of energy eigenstates as shown in Fig. 9b we have calculated the spectral dependence of gain for different densities of injected carriers. The results are shown in Fig. 11. Above the concentration of about $N_{inj} > 6.10^{18} \text{cm}^{-3}$ the gain spectrum shows the contribution from n = 2 electron states. The structure visible in the low energy tail of the gain spectrum refers to e-hh and e-lh transitions, respectively. For $N_{inj} > 10^{19} \text{cm}^{-3}$ the gain spectrum
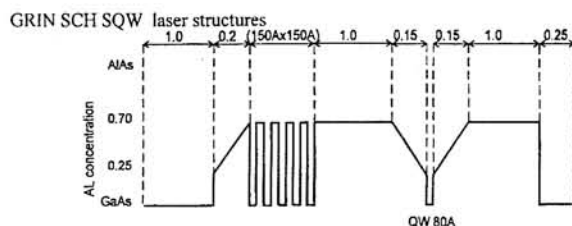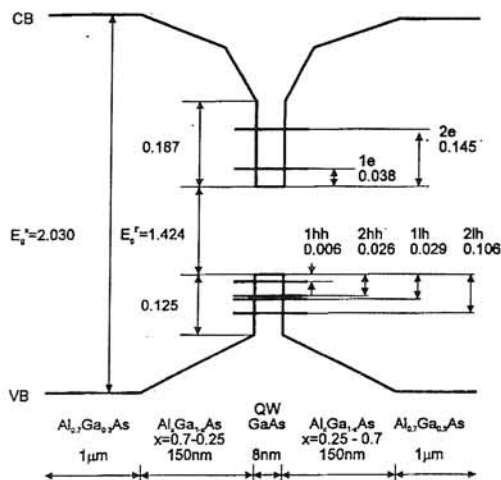

Fig. 9. GRIN SCH SQW laser structure (a); band profile of the active region with quantized energy states (b).

becomes very wide, dominated by n = 2 transitions. At the onset of second quantized level gain is almost doubled due to the added contribution of n = 2 transitions. Whether in real device the second quantized state will come into play depends on the length of the laser. By tracing the peak of the gain spectrum as a function of injected carrier density (or quasi-Fermi level) as indicated in Fig. 12 the lasing energy (wavelength) as a function of the above can be obtained. The lasing wavelength characteristics are accompanied by an extraordinary increase in threshold current density with increasing gain (that is, decreasing laser length). Fig. 13 shows that to get threshold current density of the order of 300Å/cm^2 the laser length of at least 400 μm is needed. Since the dependence of threshold current density on the cavity length saturates easily, further increase of the laser length makes sense only when internal losses are kept low (lower than the distributed mirror losses). Otherwise the differential quantum
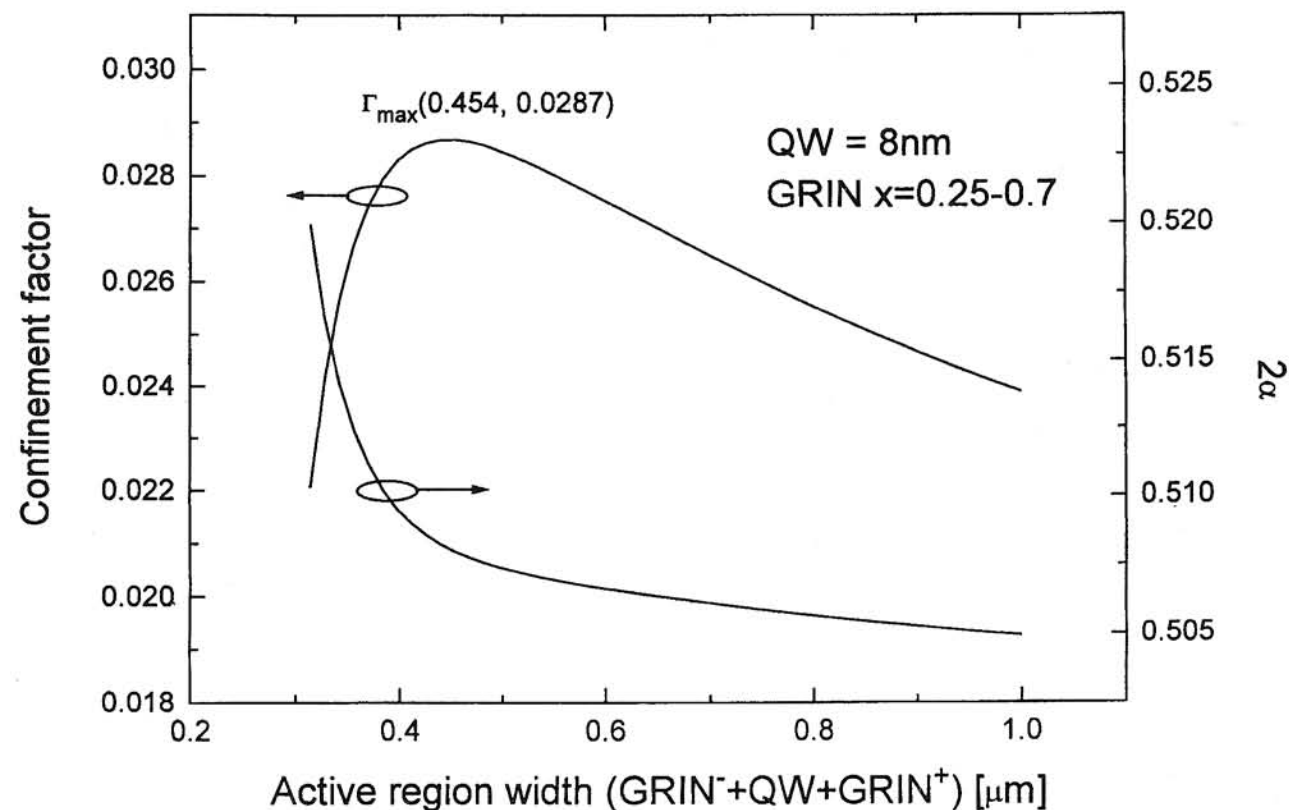
Fig. 10. Transverse mode confinement factor Γ for GRIN SCH SQW laser shown in Fig. 9.
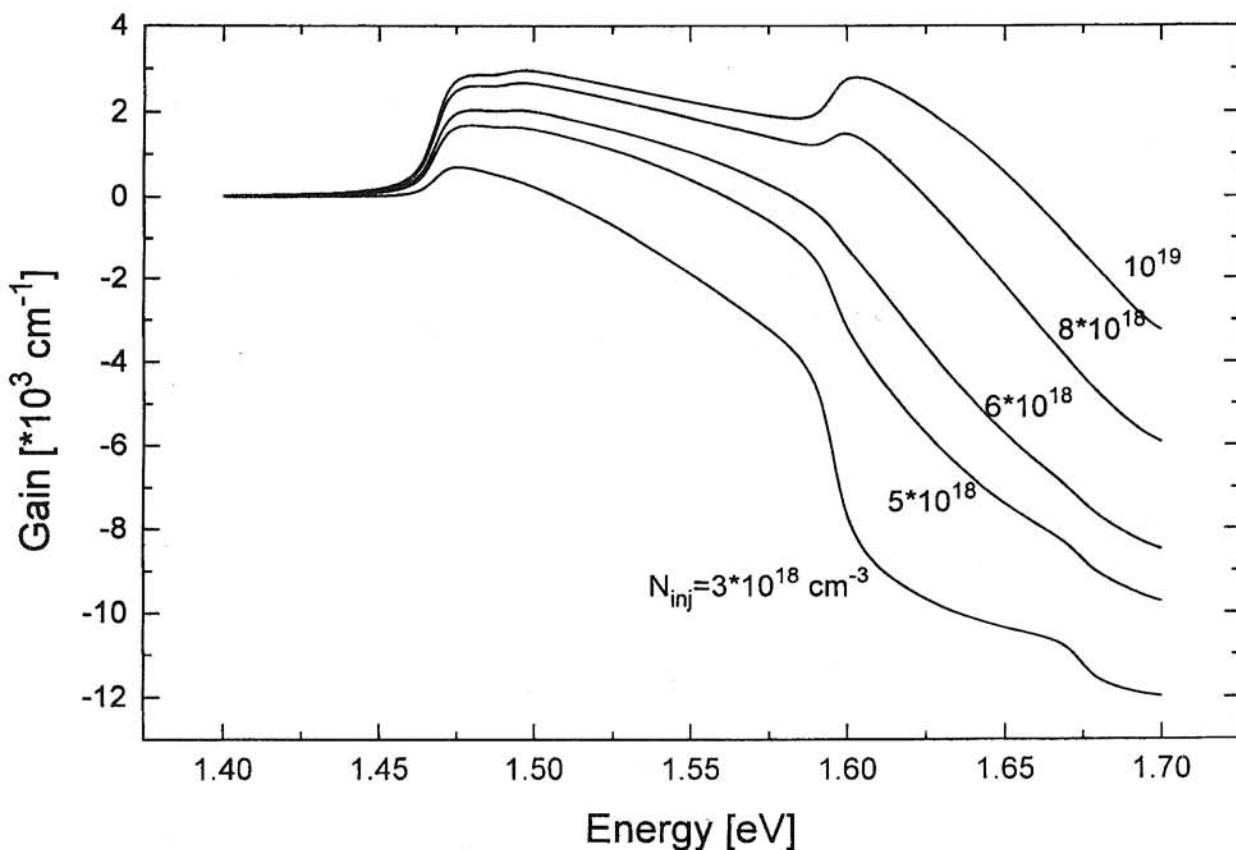
Fig. 11. Spectral dependence of gain in GRIN SCH SQW laser shown in Fig. 9.
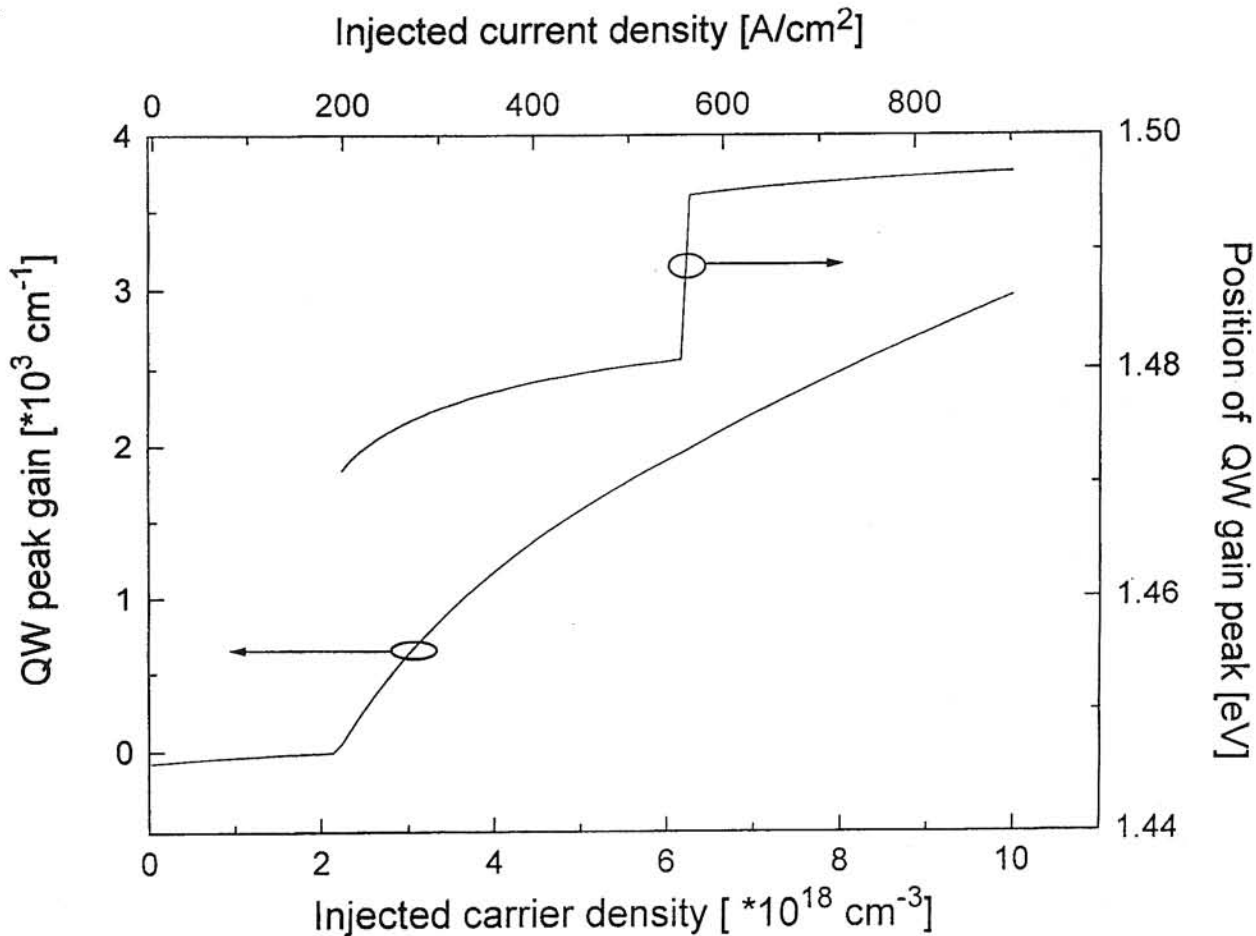
Fig. 12. The lasing energy and QW peak gain vs. the injected carrier density for GRIN SCH SQW laser shown in Fig. 9.

efficiency of the laser will be deteriorated. Generally in broad contact GaAs/AlGaAs devices one should not exceed 1 mm cavity length. On the other hand too short cavities should be avoided because of the mentioned increase of the threshold current due to the increased contribution from the end losses. The discontinuity of the $J_{th}(L)$ derivative for L slightly below 200 μm, seen in Fig. 13, is due to involvement of second (n = 2) quantized level. The greatest advantage of the simple gain model outlined above is the possibility to use it to examine the potential performance of various device structures. It also allows to study the threshold characteristics as a function of junction temperature. The simplicity of the model should not, however, overshadow the need of its further refinement.

4.3. Many-body gain theory in quantum wells

The above theory of gain involving Fermi's Golden Rule considers each electron in isolation as it interacts with electromagnetic field, i.e., it is a single-particle theory and as such it neglects mutual interactions between electrons. The physical consequences of many-body effects in dense electron plasma in QWs were already considered in preceding paper [23]. Here we will discuss briefly how do they influence gain characteristics of quantum well lasers.

The many-body interactions to be considered in this context are basically of two types: excitonic effects and bandgap renormalization effects. The first one will result essentially in the changes of
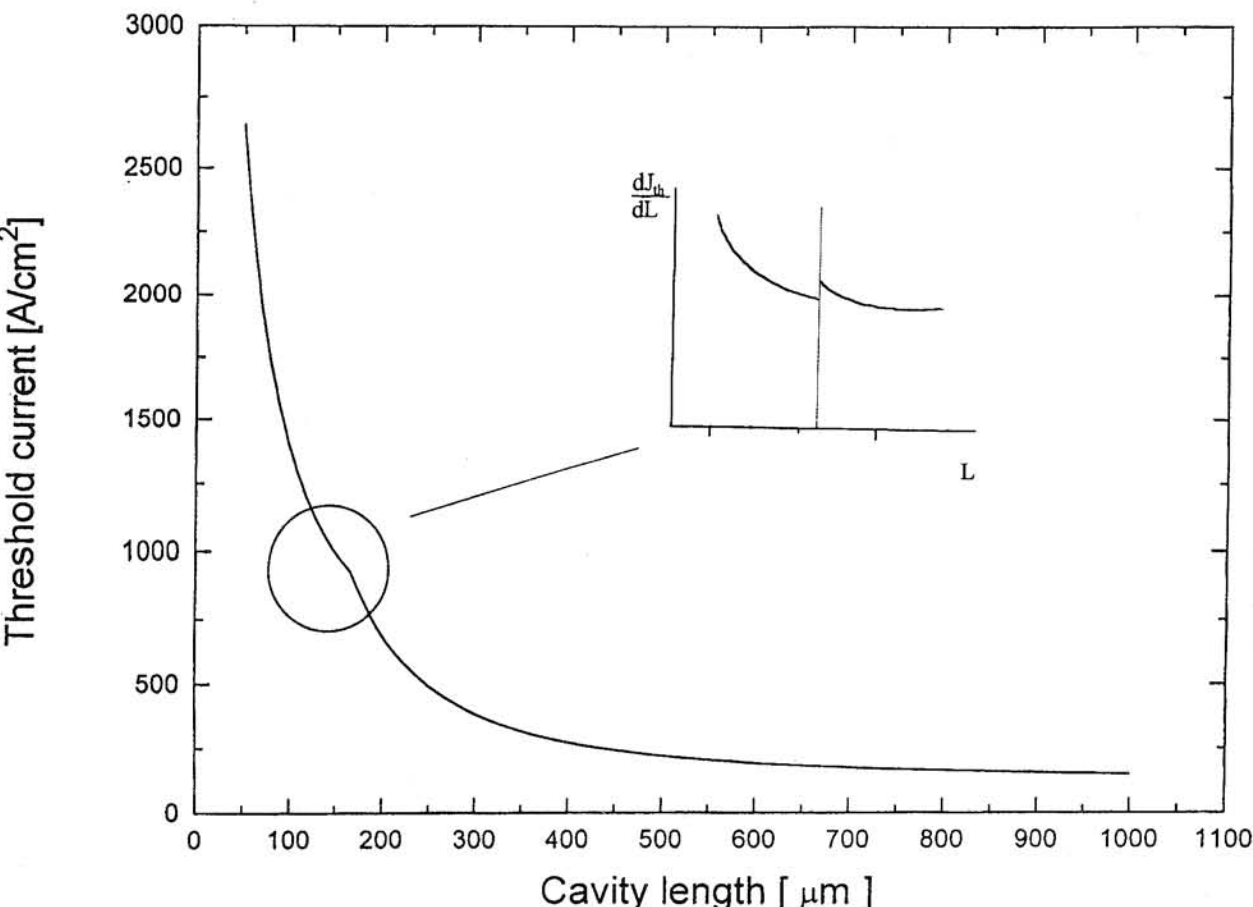
Fig. 13. The threshold current density vs. the cavity length for GRIN SCH SQW laser shown in Fig. 9.

the spectral shape of material gain curves and will be enhanced in quantum wells comparing to the bulk material. The bandgap shrinkage due to the combined exhange and correlation effects can be expressed by phenomenological relation:

$$\Delta E_F = -cN^{1/3} \qquad (10)$$

where N can be either two- or three-dimensional carrier density. A common value used for the bandgap shrinkage constant in bulk materials (assuming $N = P$), which also falls within the measured range for quantum wells, is

$$c \cong 32\text{meV}/(10^{18}\text{cm}^{-3})^{1/3} \quad \text{(bulk GaAs)} \qquad (11)$$

$$c \cong 32\text{meV}/(10^{12}\text{cm}^{-3})^{1/3} \quad \text{(GaAs/AlGaAs QWs)} \qquad (12)$$

Equations (10)−(12) are not entirely accurate, in particular for quantum wells for which there is

some experimental and theoretical uncertainty in both the one-third power law and the value of c [24]. The net effect of the bangap shrinkage is the noticable red-shift of gain spectrum accompanied by its reshaping and enhancement. This phenomenon is clearly observable in quantum well lasers where the high threshold carrier density shifts the lasing wavelength beyond the known band edge wavelength of the quantum well.

A rigorous treatment of the many-body Coulomb interactions in a quantum well lasers uses semiconductor Bloch equations and makes the quasi-equilibrium approximation to derive expressions for the gain [25]. It differs from the above presented phenomenological approach, which is indeed a free-carrier theory with *ad hoc* inclusion of band gap renormalization, by a proper treatment of Coulomb enhancement (correlation) effects. For disscusion of these effects the reader is referred to paper [23]. The results of full many-

-body calculations of quantum well gain for different injected carrier densities are compared with the results of simple free-carrier theory neglecting bandgap renormalization and Coulomb enhancement in Fig. 14a. As discussed earlier the band-edge effects are more pronounced in quantum wells because of the step like instead of square root energy dependence of the density of states. Besides the red shift of the gain curve there is a substantial reshaping of the high energy part of the gain spectrum. This is shown in Fig. 14b where the net effect of Coulomb enhancement on gain spectrum is illustrated.

5. Conclusions

The ultimate test of the technology are devices. To demonstrate the achieved level of molecular beam epitaxy the test lasers were fabricated at various stages of technology development. The laser structures were designed according to the set of rules presented in this article. The broad contact (50 μm or 100 μm stripe width) lasers were fabricated from GRIN SCH SQW structures using standard processing used previously for DH lasers. The lasers with cavity length varying from 200 μm to 900 μm were prepared by cleaving. The AuGe-Ni/Au contact with additional thick Au layer was used for n-side of the device and Cr (200Å) Pt (1000Å) contact, again with Au layer was used for p-side. The lasers were mounted p—side up on copper blocks.

The devices were operated in pulsed regime and continuously at room temperature. The lasers showed good differential quantum efficiencies, low internal absorption losses and linear, kink free characteristics. The first lasers exhibited the average threshold currents ($\sim 1500 A/cm^2$), much higher than theoretically predicted ($\sim 500 A/cm^2$) which was attributed to bad quality of AlGaAs emitters. The substrate temperature of 630°C used at the begining turned out to be much to low to obtain good quality AlGaAs. Also V/III beam ratio, which for the first structures was equal to 10 during the whole growth process had to be optimized. The essential improvement of the laser parameters has been obtained by rising the substrate temperature to 700°C and optimizing III/V ratio during the growth of different layers of the structure. As a result, the CW room-temperature GRIN SCH SQW lasers (λ = 820 nm), with extrapolated threshold currents densities as low as 350A/cm^2 and internal quantum efficiencies of 96% were produced [9]. The lasers represent state-of-the-art in technology of this type of devices. Over the past decade, laser diodes have become, a central design element in many optoelectronic devices. With their increasing complexity, especially in the case of quantum well
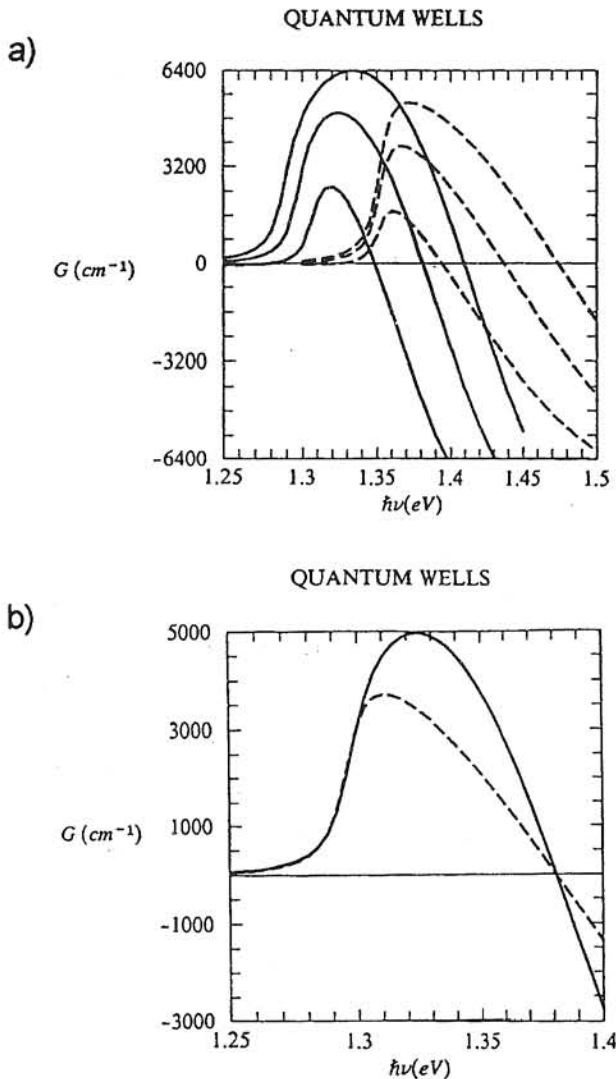

Fig. 14. Quantum well gain for injected carrier densities N = 2x10^{18}cm^{-3}, 3x10^{18}cm^{-3} and 4x10^{18}cm^{-3} in order of increasing peak gain according to many body theory (solid lines) and free-e-carrier theory (dashed lines) (a) and Coulomb enhancement effects on gain according to many body theory (solid lines) and free—carrier theory (dashed lines) (b). [quoted after ref. (25)].

devices, the costs of their manufacturing were running high. Therefore, to avoid numerous fabrication runs the device modelling should be used to assist in the development process. This is the reason why we pay so much attention to development of the design rules and more advanced numerical simulators of the lasers [26−30].

References

1. Quantum Well Lasers, (Ed. P.S.Zorry, Jr., Academic Press, Boston, 1993).

2. M.A. Herman, H. Sitter: *Molecular Beam Epitaxy: Fundamentals and Current Status*, Springer-Verlag, Berlin, 2nd edition, 1996.

3. H.C. Casey, Jr., M.B. Panish: *Heterostructure Lasers*, Academic Press, New York, 1978.

4. B. Mroziewicz, M. Bugajski, W. Nakwaski: *Physics of Semiconductor Lasers,* North Holland, Amsterdam, 1991.

5. M. Rosenzwaig, M. Mohrle, H. Duser, H. Venghaus, IEEE J. Quantum Electron., QE−27 (1991) 1804.

6. M. Bugajski, M. Kaniewska, K. Regiński, A. Maląg, S. Łepkowski, J. Muszalski, SPIE Proceedings, *Laser Physics and Technology*, 1997.

7. S.R. Chinn, P.S. Zorry, A.R. Reisinger, IEEE J. Quantum Electron., QE−24 (1988) 2191.

8. M. Kaniewska, K. Regiński, A. Barcz, S. Kasjaniuk, J. Kątcki, Electron Technology, 29, 2/3 (1996) 143.

9. M. Kaniewska, K. Regiński, J. Muszalski, D. Kryńska, A. Litkowiec, M. Bugajski, Electron Technology, 29, 2/3 (1996) 131.

10. M. Kaniewska, K. Regiński, J. Muszalski, D. Kryńska, A. Litkowiec, J. Kaniewski, M. Wesołowski, M. Bugajski, Acta Physica Polonica A90 (1996) 847.

11. M. Bugajski, M. Kaniewska, K. Regiński, J. Muszalski, D. Kryńska, A. Litkowiec, Electron Technology, 29 (1996) 4.

12. M. Bugajski, M. Kaniewska, K. Regiński, A. Maląg, Abstract Book of 5th Symposium on Laser Technology (STL), Szczecin−Świnoujście (1996).

13. G.J. Davies and D. Williams, in E.H.C. Parker (ed.): *The Technology and Physics of Molecular Beam Epitaxy*, Plenum, New York, (1985) p. 38.

14. L.L. Chang, K. Ploog, (eds.): *Molecular Beam Epitaxy and Heterostructures,* NATO ASI Series, Series E: Applied Sciences, No.87 (Nijhoff Boston 1985).

15. K. Regiński, J. Muszalski, V.V. Preobrazhenskii, D.I. Lubyshev, Thin Solid Films, 267 (1995) 54.

16. V.V. Preobrazhenskii, D.I. Lubyshev, K. Regiński, J. Muszalski, Thin Solid Films, 267 (1995) 51.

17. W.T. Tsang, Appl. Phys. Lett., 40 (1982) p. 217.

18. D.K. Wagner, R.G. Waters, P.L. Tihanyi, D.S. Hill, A.J. Roza Jr., H.J. Vollmer, M.M. Leopold, IEEE J. Quantum Electron., QE−24 (1995) 1258.

19. P.W.A. McIllroy, A. Kurobe, Y. Uematsu, IEEE J. Quantum Electron., QE−21 (1985) 1958.

20. W.X. Zou, J.L. Mertz, L.A. Coldren, J. Appl. Phys., 72 (1992) 5047.

21. M. Yamanishi, I. Suemune, Jap. J. Appl. Phys., 23, (1984) L35−L36.

22. C.S. Chang, S.L. Chuang, IEEE J. of Selected Topics in Quantum Electron., 1 (1995) 218.

23. M. Bugajski, K. Regiński, Optoelectronics Review, *this issue*.

24. S. Das-Sarma, R. Jalabert, S.R. Eric Yang, Phys. Rev. B 41 (1990) 8288.

25. W.W. Chow, S.W. Koch: *Semiconductor-Laser Physics*, Springer Verlag, Berlin (1994).

26. S.P. Łepkowski, B. Mroziewicz, Electron Technology, 28 (1995) 29.

27. S.P. Łepkowski, Electron Technology, 29 (1996) 29.

28. S.P. Łepkowski, B. Mroziewicz, Electron Technology, 29, (1996) 394.

29. D. Radomska, M. Bugajski, Electron Technology, 29 (2/3) (1996) 94.

30. S.P. Łepkowski, M. Bugajski, Electron Technology, 29 (1996) 88.